Influence of powder recycling on 316L stainless steel feedstocks and printed parts in L-PBF

Timothée Delacroix, Fernando Lomello, Frédéric Schuster, Hicham Maskrot, Jean-Paul Garandet

Influence of powder recycling on 316L stainless steel feedstocks and printed parts in laser powder bed fusion

Timothée Delacroix[a,*], Fernando Lomello[a], Frédéric Schuster[b], Hicham Maskrot[a], Jean-Paul Garandet[c]

[a] Université Paris-Saclay, CEA, Service d'Études Analytiques et de Réactivité des Surfaces, 91191, Gif-sur-Yvette, France
[b] Université Paris-Saclay, CEA, Cross-Cutting Program on Materials and Processes Skills, 91191 Gif-sur-Yvette, France
[c] Université Grenoble Alpes, CEA, LITEN, DTNM, F-38000 Grenoble, France

[*] **Corresponding author:** Timothée Delacroix – timothee.delacroix@cea.fr

Abstract

In Laser Powder Bed Fusion (L-PBF) of metallic materials, costs and material yield strongly depend on the ability to reuse powder efficiently, as a significant amount is not solidified as part by the laser beam. However, some of the powder is nevertheless exposed to high temperatures during the manufacturing process resulting in an alteration of the feedstock properties if reused. Therefore, there is a need to study and understand powder degradation during the L-PBF process and its direct effects on the printed parts. In this study, gas-atomized 316L stainless steel powder was used, recovered, sieved and reused up to 15 times in order to produce successive L-PBF prints without adding any virgin powder. Both recycled powders and elaborated parts were fully characterized at each iteration to investigate changes in particles (morphology, rheology, microstructure and chemical composition) as well as printed parts (porosity, microstructure, microhardness and tensile properties). Recycled powder exhibited larger particle size and an improved flowability. A gradual increase in oxygen content was observed, along with the presence of colored and oxidized particles, as well as magnetic particles. Parts density slightly decreased with powder reuse and their microstructure featured more numerous and finer grains along reuse cycles. On the other hand, no significant difference was found on the microhardness and the tensile properties of the L-PBF components.

Keywords: Laser Powder Bed Fusion, Powder recycling, Stainless steel, Powder characterization, Mechanical properties

1. Introduction

Additive Manufacturing (AM) regroups a number of processes that allow to create parts from three dimensional (3D) model data by successive additions of material, as described by the ISO-ASTM 52900-15 norm [1]. As opposed to conventional processes, AM offers the possibility to manufacture complex parts and to use only the right amount of material needed to produce them [2]. Laser Powder Bed Fusion (L-PBF), also often called Selective Laser Melting (SLM), is one of the most widely used AM technology and can process a wide range of metallic materials such as stainless steels, maraging steels, nickel superalloys, titanium alloys or aluminum alloys [3]. In this process, a thin layer of powder (20-90 µm) is spread by a recoater on a build platform, then a laser beam selectively melts

the particles and the molten metal solidifies rapidly. The repetition of these operations, layer upon layer, with the laser scanning following trajectories predefined with the slicing of the digital file, leads to the production of 3D parts. The design freedom allows to achieve mass reduction of structures with the use of topology optimization, and also to limit assembly operations by replacing several parts with an integrated assembly. In addition, mechanical properties of parts elaborated by L-PBF are equivalent or superior compared to those of conventional processes due to the fast cooling rates and the resulting fine microstructures [4][5]. However, inconsistencies of printed parts quality in terms of porosities, cracks and surface roughness are still common [6].

L-PBF is a complex process, which involves numerous phenomena and parameters, and most of the efforts have been focused on the optimization of the process to improve components quality. Machine parameters such as the laser power, scanning speed and strategy, hatch distance and layer thickness (Fig. 1a) directly affect the melt pool size, shape and instabilities, solidification rate and resulting microstructure of the elaborated parts [7][8].

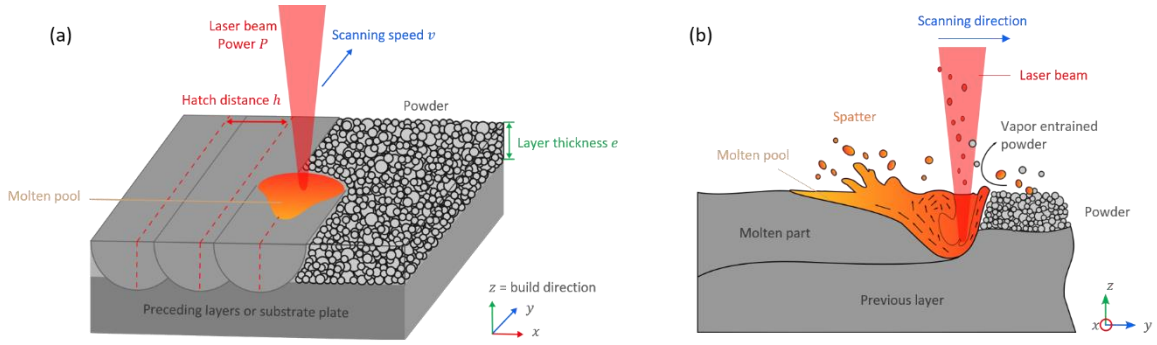

Fig. 1. (a) Schematics of L-PBF process parameters, (b) Formation of spatter particles

Along with the process parameters, the effect of the raw material characteristics, *i.e.* the metallic powders in the case of L-PBF, is an important issue to assess in order to produce reliable parts and improve process repeatability. This relation between powder and final components properties is less studied in the literature, even though changes in powder characteristics can lead to the formation of metallurgical defects [9–12]. During the process, only a small fraction of the powder is fused by the laser beam and solidified as part. The price of the feedstock being high, there is a need to reuse the non-melted powder to maximize the resource efficiency of the L-PBF technology [13–15]. However, powder leftover properties may deviate from those of the virgin material after being subjected to the L-PBF environment. The reuse of the powder, also referred to as recycling, can lead to a deterioration of the final parts properties. Therefore, understanding the impact of powder recycling on both powder and printed parts is essential.

From a general point of view, powder degradation in L-PBF can often be related to its exposure to a high temperature environment. This occurs for instance when spatters are ejected from the molten pool and recovered on the powder bed. Such instabilities can in turn be related to liquid state instabilities, driven by the recoil pressure caused by the evaporation of some alloying elements [16]. In addition, Marangoni convection coming from temperature-related surface tension variations at the melt pool surface can also lead to fluid flow instabilities. In addition to these liquid pool spatters, the vaporization flow can also drive the entrainment of surrounding virgin particles through the laser beam [17–19], as schematized in Fig. 1b. Liquid pool spatters can generally be sieved out, but not the entrained powder. In any case, contamination of the powder-bed surrounding the solidified parts by these spatter particles is one reason of the alteration of powder properties with recycling. Apart from spatter related degradation, Pinto et al. [20] distinguished a second group of unused powder close

enough to the heat source to be subjected to modifications. The latter consists of particles in the heat-affected zone (HAZ) in the near vicinity of the molten pool.

Successive recycling in L-PBF leads to an increase of the proportion of altered particles among the recovered powder, and changes in particles morphology, chemical composition or microstructure can be observed. Not all recycling studies in the literature show identical results but tendencies emerge. Particle size distribution (PSD) seems to shift towards larger values with intensive reuse, with an increase of irregularly-shaped particles [21–23]. Smaller amounts of fine particles are also reported, which can lead to an improved powder flowability, as it reduces frictions and inter-particle adhesion. On the other hand, less spherical particles are expected to negatively affect the flow behavior of a powder [21,24–26]. An increase of oxygen content in reused powder has been repeatedly observed [27,28]. Some materials such as titanium or aluminum alloys are more prone to oxygen pickup but this phenomenon has also been noticed on stainless steel powders. In the case of stainless steel 316L, several authors noticed the presence of silicon and manganese oxides on the surface of spatter particles, that can be held partly responsible for the change in oxygen content [29–31]. Microstructural modifications can also occur on these particles. For example, Heiden et al. [29] showed an increase of the volume fraction of δ-ferrite phase from 0-0.5 % to 6-7 % in SS316L powder reused 30 times. These magnetic particles can lead to particles clustering and negatively affect the powder bed uniformity during L-PBF [20]. Regarding both liquid spatters and magnetic particles, a large proportion of altered powder can be removed by a sieving process, but some of it still passes through. Conclusions on the influence of powder recycling on printed parts are not that straightforward. Sartin et al. [32] studied SS316L components produced with powder recycled 12 times and found slight variations and no statistical trends regarding specimens density, chemical composition, mechanical strength, ductility or microhardness. Other studies highlighted minor changes in terms of yield strength (YS) and ultimate tensile strength (UTS) [33], but elongation at break has been shown to decrease with recycled powder [23,25,34]. All these properties depend on the attributes of the powder but are also correlated to the L-PBF processing conditions, which can lead to different results on the parts.

As L-PBF has captured the attention of many industrial sectors such as aerospace, biomedical, automotive or nuclear, an in-depth understanding of powder recycling and its effects on the final components properties is necessary for a widespread adoption of the technology. A number of studies have been carried out on different materials but most of them focus on the comparison of the virgin condition and a recycled state. The purpose of the present work is to assess both the powder feedstock degradation and the effect on printed specimens throughout multiple recycling using standard SS316L as base material. It should be stated that 316L is not considered in view of a specific application field. Indeed the material is widely used in a number of industrial domains, including the energy, medical and nuclear sectors, but even though specifications for reuse may differ from one industrial sector to another, the issue of recycling remains. The evolution of properties will be followed throughout each printing cycle, with the characterization of both powder attributes and final parts properties. A detailed investigation is conducted on the recycling of gas-atomized stainless steel 316L powder and its impact on parts elaborated with optimum process parameters in L-PBF. Systematic characterization of the powder is carried out by means of laser granulometry, inert gas fusion, flowmeter funnels, microscopies and X-ray diffraction. Solidified specimens features such as density, oxygen content, microhardness and tensile properties are examined after each of the 15 printing cycles performed without addition of fresh powder.

2. Materials and methods

2.1. Material and L-PBF process

Gas-atomized AISI 316L powder manufactured by Oerlikon Metco Europe GmbH with a particle size distribution of 20 – 45 µm was used for this study. Table 1 shows the average chemical composition of the virgin stainless steel powder measured by inductively coupled plasma atomic emission spectrometry (ICP-AES), glow discharge mass spectrometry (GD-MS) and inert gas fusion. The observed composition fits within the range of the ASTM A240 norm [35] for SS316L, also reported in Table 1. There is no specification regarding the oxygen content, nevertheless typical values are usually less than 1000 wppm for gas-atomized products.

Table 1. Chemical composition of the virgin SS316L powder, in wt.%

Element	Fe	Cr	Ni	Mn	Mo	Si	C	P	S	N	O
Powder	Bal.	17.5	12.6	1.5	2.4	0.04	0.02	0.002	0.001	0.07	0.048
ASTM A240	Bal.	16-18	10-14	≤2	2-3	≤0.75	≤0.03	≤0.045	≤0.03	-	-

Specimens were produced on a TruPrint series 1000 L-PBF printer (TRUMPF GmbH) with a 200 W continuous Yb-fiber laser (1064 nm wavelength) and a spot size of 55 µm. Fabrication was performed under argon atmosphere with a residual oxygen concentration inside the build chamber imposed under 300 ppm. Cubic samples (10 x 10 x 10 mm^3) and horizontal cylindrical samples (Ø 10 mm x 40 mm) for mechanical tests were built using a layer thickness of 30 µm and a laser scanning strategy with a 67° rotation between layers. Laser parameters were optimized beforehand with a statistical design of experiments (DOE) on the same virgin powder batch allowing to achieve very low porosity (> 99.9 %). Parts were built with a laser power of 165 W, a scanning speed of 950 mm/s and a hatch distance of 50 µm.

2.2. Powder recycling methodology

Fig. 2 illustrates the approach used to study the impact of SS316L powder recycling on both powder feedstock and elaborated parts. 15 printing cycles followed this loop, with no addition of virgin powder during the successive fabrications. After each cycle, powder sieving was performed on the recovered powder in a Retsch AS 300 vibratory sieving station using a 50 µm screen.

Build plates were composed of 6 cubic samples, 3 horizontally built cylindrical specimens (dimensions just given above) for tensile testing and 4 vertically built cylinders to ensure that the whole powder set is subjected to machine processing at each iteration. The latter were not tested but were built to control the height of the fabrications, which was consequently decreased after each powder reuse as less powder was available after parts solidification, powder sieving and powder sample collection. Therefore, the percentage of melted volume in the build area increased gradually with recycling, going from 6 % to 22 %.

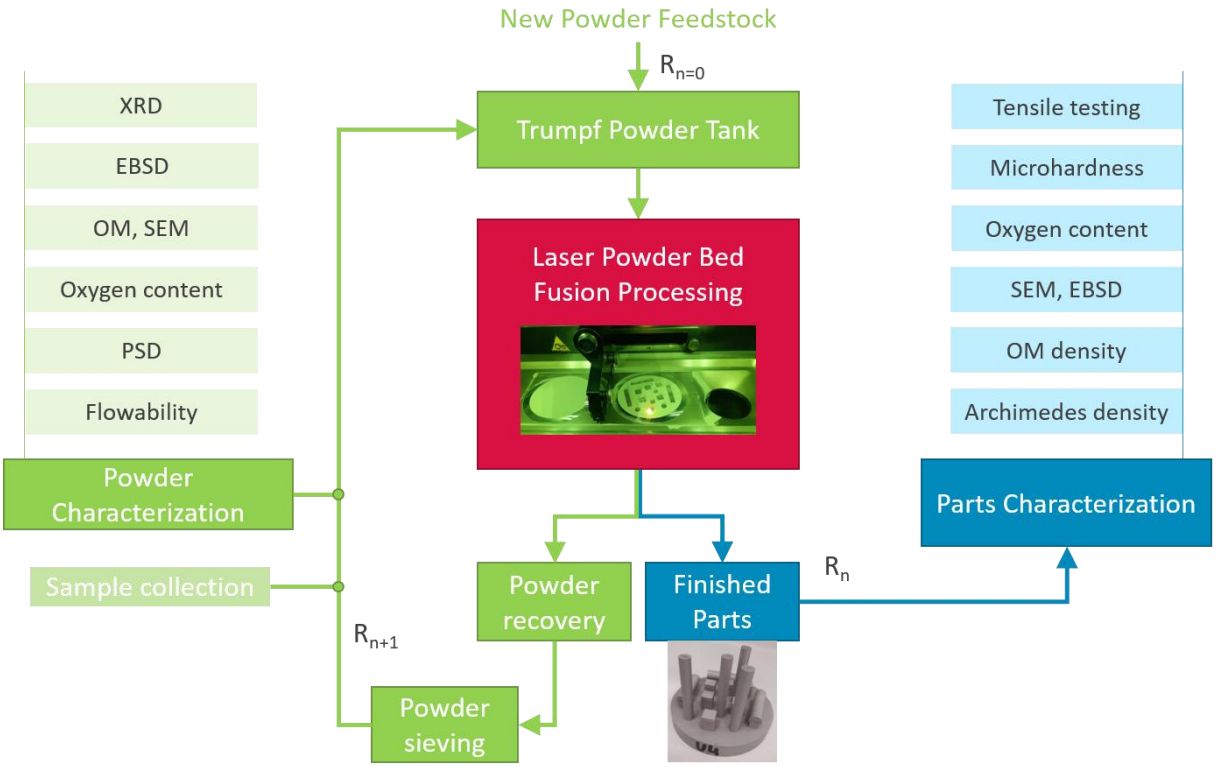

Fig. 2. Chart of the powder recycling methodology

2.3. Powder characterization methods

Optical microscopy (OM, ZEISS Axio Imager 2) and scanning electron microscopy (SEM, JEOL JSM-7000F) were used to observe particles color and morphology. X-ray energy spectra using energy dispersive spectroscopy (EDS) allowed to evaluate the surface composition of the particles. After preparation of powder samples embedded in epoxy and polished down to a 0.04 µm colloidal silica solution finish, electron backscatter diffraction (EBSD) was used to examine the microstructure, grain size and phase composition. X-ray diffraction (XRD) also helped tracking changes in powder microstructure with phase analyses obtained with a Bruker D8 Advance spectrometer. XRD data were collected after scans conducted over an angular range of 20 - 120° using a step size of 0.02°, with a Cu Kα radiation source under 40 kV voltage and 40 mA current. MAUD (Materials Analysis Using Diffraction) software was used to perform Rietveld refinement for quantification of phases [36].

Laser granulometry was used to determine the particle size distributions (PSD), with the granulometer Horiba Partica LA-950. Three to five measurements of at least 5000 particles were performed for each condition. Chemical composition was measured by ICP-AES for major elements and by GD-MS for traces (X7 Series, Thermo Fisher Scientific). Inert gas fusion with Horiba EMGA 820 AC analyzer was performed to obtain the oxygen content of the powders. Three replications were conducted at each iteration of the study to estimate statistical variations within the powder. The measurement of powders flowability was conducted using the Carney flowmeter funnel according to the ASTM B212-17 [37].

2.4. Parts characterization methods

Two methods were implemented to determine L-PBF cubic samples density. First, the Archimedes method was used [38]. Masses of each cube were measured independently three times in air and water with the help of an electronic balance with an accuracy of 0.1 mg. All samples were then analyzed by image analysis of a cross section (parallel to the build direction) after metallographic preparation, with images captured and assembled over the entire 1 cm² area with OM at a magnification of 50X. Quantification of samples porosity was then performed using ImageJ software. To investigate the parts microstructure, SEM observations and EBSD were performed on those cross sections after electrolytic polishing in a 10% oxalic aqueous solution for 30 seconds at 15 V. As for the powders, the oxygen content of the parts was measured by inert gas fusion with three to five measurement per condition.

Vickers microhardness (HV) measurements under a load of 1 kg were also conducted on the cubic samples using Struers DuraScan 70 microhardness tester. For each sample (6 per recycling), 15 measurements were taken in the diagonal of the cross section. To investigate the tensile properties of the parts produced with recycled powder, tensile specimens were machined from the cylindrical components. The specimen dimensions presented in Fig. 3 were determined according to the ISO 6892-1 standards [39]. Three uniaxial tensile tests per fabrication were carried out at room temperature using MTS Criterion 43 electromechanical test system at a displacement-controlled loading rate of 1 mm/min.

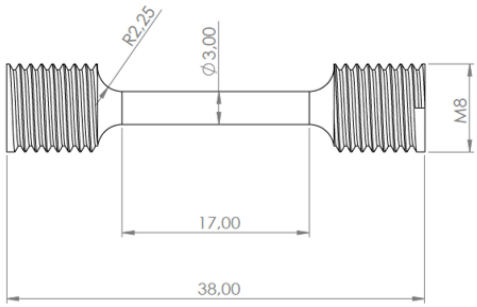

Fig. 3. Schematic of tensile specimens dimensions (in mm)

3. Results and discussion

3.1. Effect of recycling on powder

Powder morphology, which relates to particles size and shape is known to have a great impact on powder bed density and thus parts quality in L-PBF [40]. Fig. 4a shows the cumulative volumic particle size distribution of powders collected after each printing cycle and sieved through a 50 µm mesh. Particles tend to be larger with recycling even if the biggest particles are removed by the sieving, as some irregular shaped elongated particles can pass through in one direction. Powder feedstock used in this study does not really contain fine particles (less than 10 µm) so the decrease in fines is not as clear as found by other authors [24] . However, D_{10}, D_{50} and D_{90} are nevertheless slightly increasing throughout multiple recycling (Fig. 4b). The sieving is clearly effective, as shown in Table 2 with the comparison of average particle size distributions for sieved powders and sieved residues (SR) after different printing cycles. In addition, it should be noticed that more powder in fraction was sieved off related to the amount of powder recovered after each cycle, going from 1.4 % to 4 % of total recovered powder. This is related to the fact that the fraction of melted volume in the

build area used in the successive cycles is increasing. When comparing the mass of SR after each fabrication according to the corresponding melted volume, the ratio remains stable over the 15 prints (average ratio of 2.1 ± 0.2). This sieving step is useful for removing really large particles, mostly spatter particles expelled from the melt pool, but also contributes to increasing the average size of the powder. As mentioned earlier, after ejection of molten metal, these spatters can fall back on the powder bed in a semi-liquid state causing the aggregation of small powder particles. These agglomerates are then discarded by the sieving process. Another explanation to the particles size increase during recycling is that smaller particles are more likely present on the build platform and solidified. Indeed, during the L-PBF process, particles larger than the layer thickness are preferentially spread past the build area by the recoater and more are collected for reuse [41].

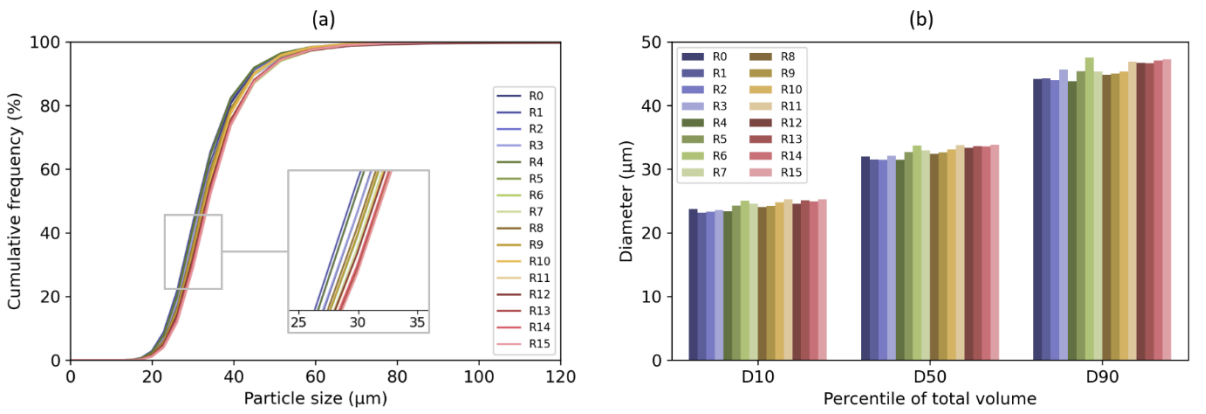

Fig. 4. (a) Cumulative particle size distributions and (b) D_{10}, D_{50}, D_{90} of powders of each printing cycle

Table 2. Average particle size distributions for recycled powders and corresponding sieved residues (SR). Numbers in parentheses are standard deviation.

Powder (Stdev)	Average diameter (µm)	D_{10} (µm)	D_{50} (µm)	D_{90} (µm)
Recycled powder after sieving				
R1	32.7 (0.5)	23.2 (0.1)	31.5 (0.3)	44.3 (0.8)
R5	34.2 (0.7)	24.3 (0.1)	32.7 (0.4)	45.4 (1.8)
R11	35.3 (1.1)	25.3 (0.5)	33.8 (0.7)	46.8 (2.5)
R15	35.4 (0.2)	25.2 (0.3)	33.8 (0.3)	47.3 (0.4)
Sieved residues (SR)				
R1 SR	85.5 (2.1)	58.5 (1.4)	80.1 (1.9)	117.8 (4.2)
R5 SR	85.6 (3.4)	58.0 (2.0)	80.3 (3.0)	118.7 (6.4)
R11 SR	91.7 (2.4)	59.7 (0.5)	84.7 (0.7)	132.2 (7.7)
R15 SR	91.5 (2.9)	58.4 (1.3)	83.2 (1.6)	135.6 (6.6)

Powder shape is also affected by the L-PBF process and particles tend to be less spherical. Fig. 5 (a) presents microscopy observations of the virgin powder and the sieved powder after 5, 10 and 15 prints, and Fig. 5 (b) shows back-scattered electron micrographs of the virgin powder and highly recycled state (R15). More agglomerates and irregularly shaped particles are visible with increase of powder reuse. A major increase of the number of colored particles (yellow-brown, blue) is also noticeable.

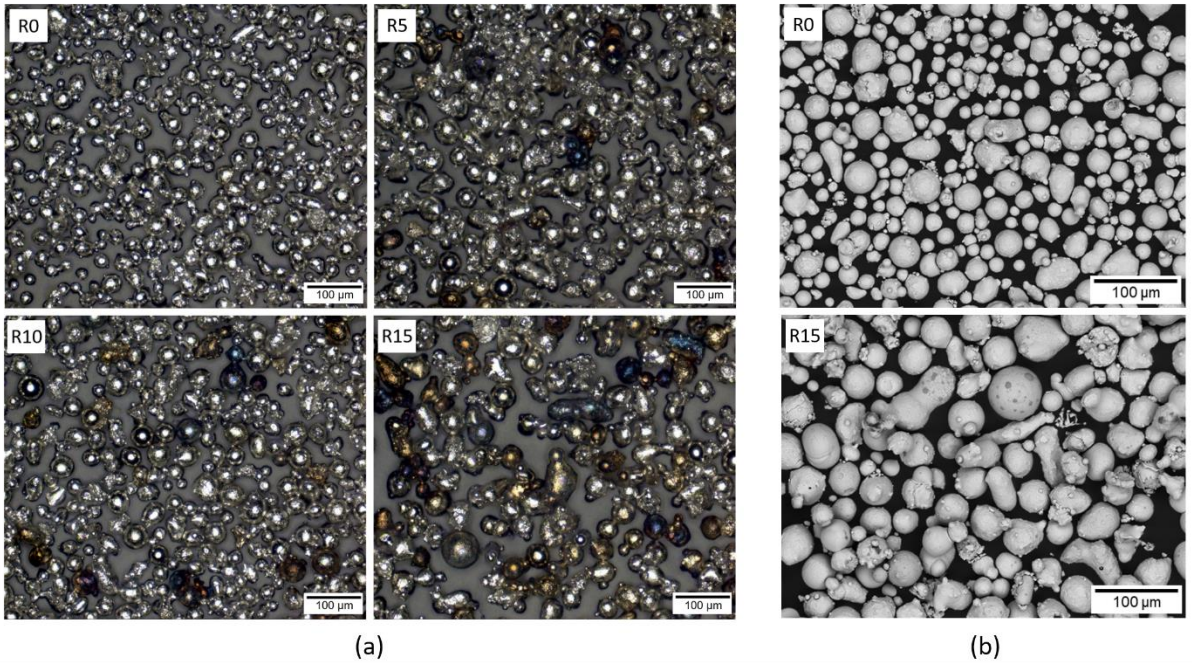

Fig. 5. (a) Optical images of R0 (virgin powder), R5, R10 and R15 powders at 200x magnification; (b) Back-scattered electron micrographs of R0 and R15 powders at 500x magnification

Rheology tests were carried out using Carney funnel to investigate the flow behavior of the powders after each printing cycle. Fig. 6 shows the evolution of powders flow times throughout recycling. An improvement of the stainless steel feedstock flowability is clear with multiple powder reuse. This is in accordance with the decrease of the number of smaller particles, which reduces inter-particles interactions [42].

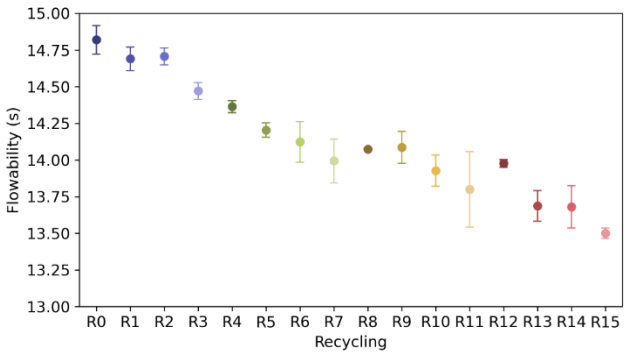

Fig. 6. Flow time of powder after each printing cycle

On top of the PSD shift toward larger values, another explanation to the shorter flow times of recycled powders despite the decrease of particles sphericity could be the presence of oxides on the surface of some particles, which can reduce friction and interparticle adhesion [24]. In the present study, the increase of colored oxidized particles could be the dominant mechanism responsible for this improved flowability rather than the decrease of fines particles, as the D_{10} of the virgin powder is already quite high (>20 µm).

Chemical composition analyses were performed on the various powder samples. No significant difference in terms of chemical composition was found between the virgin and highly recycled powders, except regarding the oxygen content. Fig. 7 shows the variation of oxygen content in the SS316L powder with reuse times. The latter gradually increases throughout the 15 iterations, from

474 ppm to 665 ppm. This increase is noticeable but oxygen concentration remains within acceptable range. In comparison, oxygen contents of SR are stable around 1600 – 1800 ppm.

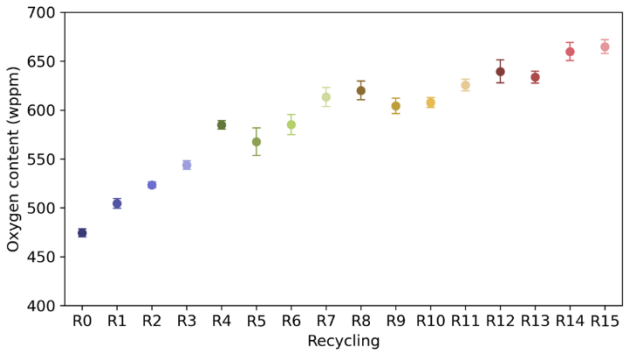

Fig. 7. Oxygen content of the powder with recycling

The oxygen pickup can in part be associated to the colored particles observed in Fig. 5. Different colors correspond to different oxide layer thicknesses and thus to different overall oxygen contents [43]. It can be assumed that these particles oxidized in the near vicinity of solidified parts, where heat transfer induces significant temperature increases. There was no size effect regarding the coloration of these particles. Other kinds of oxygen-affected particles were observed in both recycled and sieved samples, by OM and SEM. Some particles present oxides nodules on their surface. EDS mapping shows that those are Mn and Si rich oxides, as shown in Fig 8.

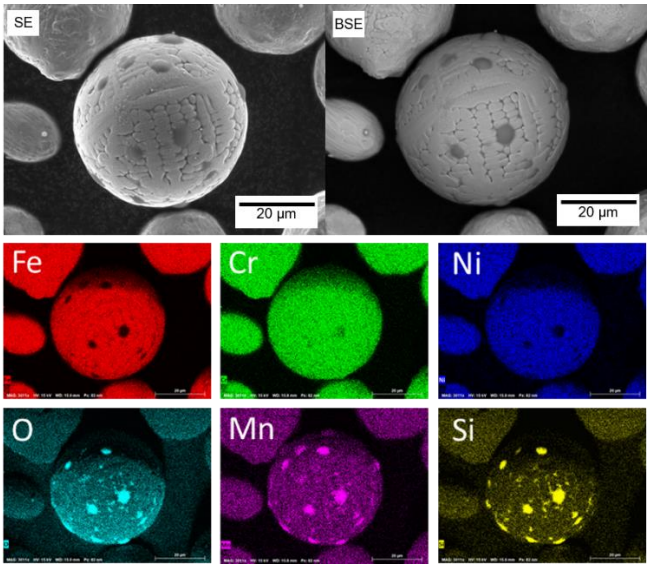

Fig 8. SEM (Secondary Electrons and Backscattered Electrons) images and EDS maps of a partially oxidized particle in the recycled powder

Similar selective oxidization is found on large spatters (over 100 µm) and by different authors who studied stainless steels ejecta [29–32]. A tentative explanation was proposed by Simonelli et al., based on the fact that Mn and Si are elements with high affinity to oxygen and greater volatility compared to Fe and Cr, resulting in increased diffusion toward the surface. Partially oxidized particles were mostly found in the SR. However, , the present findings show that some of them are small enough to pass through the 50 µm sieving mesh and were found even after only one print. The latter could be vapor-entrained powders, *i.e.* virgin particles entrained with sufficient momentum from the surrounding of the melt pool by the vaporization flux to pass through the laser beam, melt fully or partially, but in all cases are submitted to a high enough temperature to oxidize in flight [44]. OM and

SEM correlations were carried out to observe the visual colors of these nodule-containing ejecta. Indeed, in the samples collected after numerous prints (10 – 15), most of these ejecta identified and observed are also colored. However, when inspecting the powder after one printing cycle and sieving, those particles do not seem to present other colors than the 'classical grey' of the virgin powder. This may mean that they could have partially oxidized in flight during one L-PBF print and then with powder reuse were heated and *colored-oxidized* during following fabrications while being in the HAZ. Fig. 9 shows different partially oxidized particles observed with both OM and SEM in back-scattered electrons mode. They all have Mn and Si rich oxide nodules, but present different surface colorations. It is important to mention that most of the colored particles do not present oxide nodules.

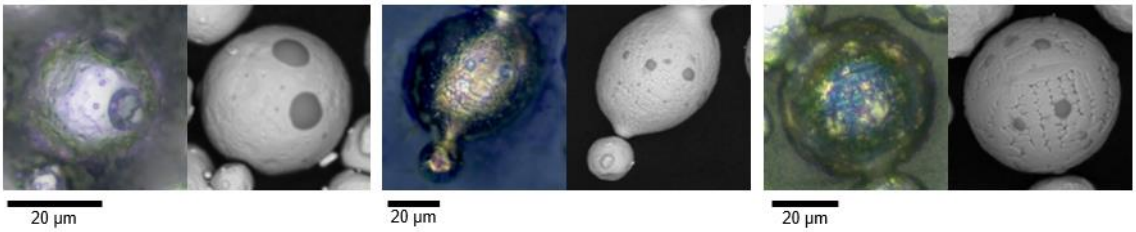

Fig. 9. OM - SEM micrographs correlation of partially oxidized particles in the recycled powder

Extremely spherical, smooth and bright particles are also noticeable in the recycled powder. These are magnetic particles, and it was therefore possible to extract them with a standard magnet to analyze them. Backscattered electrons observations reveal the presence of dark regions on the surface, which are also richer in O, Mn and Si. EDS point analyses were used as semi-quantitative analysis to compare the oxides of the two kinds of particles (magnetic and partially oxidized). Oxide elements concentrations (in weight %) of the magnetic particles are less important (O ~ 17 %, Mn ~ 10 % and Si ~ 7 %) than those of the non-magnetic (O ~ 35 %, Mn ~ 25 % and Si ~ 15 %). EBSD performed on these powders shows that the magnetic particles are fully ferritic and single crystals. All other particles are austenitic and polycrystalline. Fig. 10a shows optical microcopy of magnetic particles with as-virgin powder attracted with them on the bottom right. Fig. 10b (taken on a different set of particles) represents EBSD images of such powders. The three ferritic particles (BCC) are single crystals of different orientations, and the austenite one (FCC) is polycrystalline.

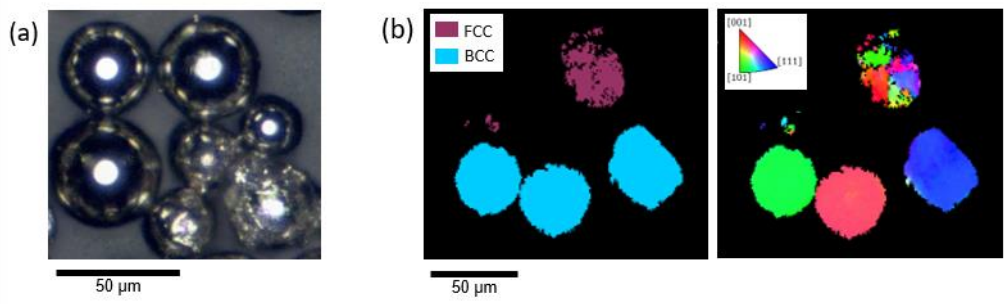

Fig. 10. (a) Optical microscopy observation of magnetic (spherical-bright) and as-virgin particles; (b) EBSD of magnetic and as-virgin particles (phase map and inverse pole figure)

According to Korinko and Malene [45], the solidification mode of austenitic stainless steels can be predicted according to the ratio of chromium equivalence (Cr_{eq}) and nickel equivalence (Ni_{eq}). Several equations are proposed by different researchers to calculate this ratio, including the WRC-1992 [46] equivalence equations (Cr_{eq} = Cr + Mo + 0.7Nb; Ni_{eq} = Ni + 35C + 20N + 0.25Cu) that were used with the chemical compositions of the virgin powder and R15 powder measured by ICP-AES and GD-MS. With Cr_{eq}/Ni_{eq} of 1.29 and 1.31 respectively, both virgin and highly recycled powders should follow an

AF solidification sequence with primary austenite then ferrite: $L \rightarrow L + \gamma \rightarrow L + \delta + \gamma \rightarrow \gamma + \delta \rightarrow \gamma$, or an A mode: $L \rightarrow L + \gamma \rightarrow \gamma$. The higher the ratio is, the larger the ferrite forming tendency. However, such a chemical composition criterion is not adequate to support the formation of fully ferritic particles in the recycled powders.

Cooling rates can also be expected to have an influence, and it can be suggested that they are high enough to cause sufficient amount of undercooling to bypass austenite nucleation and form metastable δ ferrite. From qualitative arguments, it can be inferred that at a given cooling flux, smaller particles will have a higher cooling rate. Conversely, at a given particle size, a higher heat exchange coefficient will result in a higher cooling rate. It can thus be proposed that the magnetic particles are particles entrained through the laser beam or melt pool spatter ejected at high velocity, as suggested by Heiden et al. [29]. Young et al. [47] found that among the different types of spatter in L-PBF, liquid droplets ejected directly from the melt pool exhibit the smallest sizes and highest velocities.

XRD was carried out after sieving to investigate the crystal structure of powder samples and perform phase quantification using Rietveld refinement. A comparison of the XRD patterns for the virgin powder and highly reused powder (R15) is showed in Fig. 11. Phase quantification highlighted the increased fraction of δ-ferrite phase after the 15 L-PBF prints, going from 0-1 wt.% to 4 wt.%.

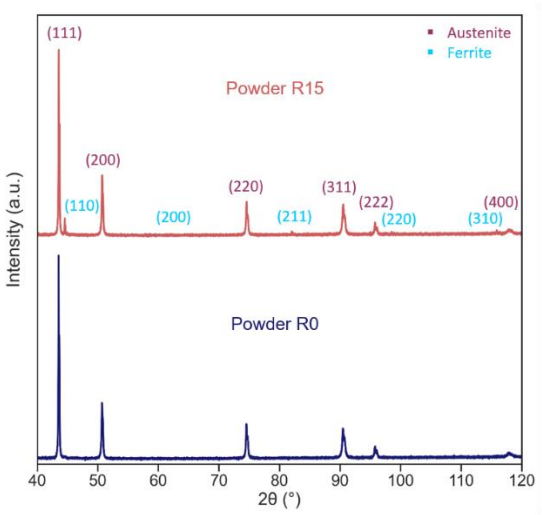

Fig. 11. XRD diffractograms of the virgin (R0) and 15-times recycled (R15) powders

EBSD analyses were also conducted on powders collected after various printing cycles. However, it is difficult to estimate the proportion of ferritic particles on the sieved samples as these images do not display numerous particles. The small diameters of the latter make it rather difficult to prepare samples with many uniformly distributed particles, some particles being expelled during polishing. In this respect, EBSD of SR were easier to implement due to their larger size. Fig. 12 shows EBSD phase maps and inverse pole figures of the 15 times recycled powder (R15) and the SR sample collected after its sieving. It is clear that ferritic particles are more abundant in the SR. Interestingly, magnetic separation in the SR showed that these smooth and spherical particles are relatively small. Fig. 13 represents an optical microscopy observation of particles extracted from SR with a standard magnet. The diameter of the smooth particles does not exceed 70-80 µm, and a majority is even smaller than 50 µm. This size would have theoretically allowed them to pass through the sieve mesh, but their magnetic attraction must have favored particles clustering and their recovery upon sieving. These limited diameters are in accordance with the supposition of fast cooling provoking the solidification of BCC ferrite, and was also reported by Pinto et al. [20].

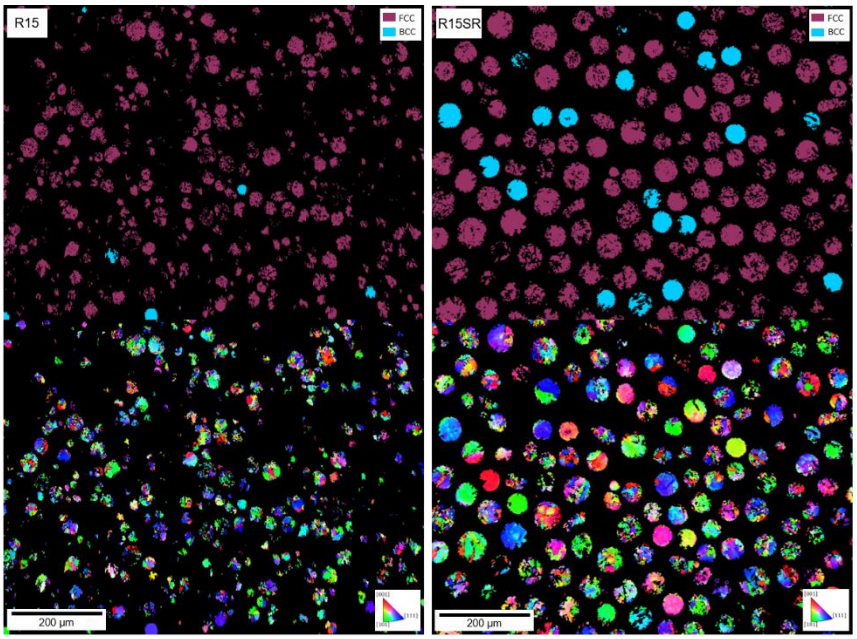

Fig. 12. EBSD phase map and inverse pole figure map of sieved recycled powder (R15) and sieved residues (R15SR)

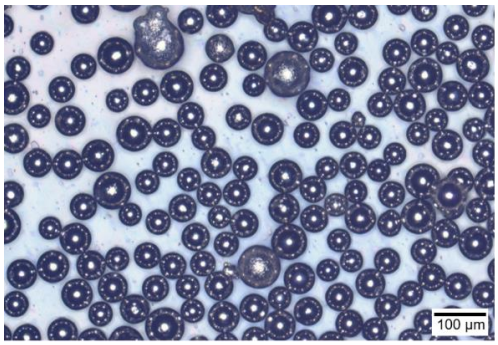

Fig 13. Optical microscopy observation of magnetic particles extracted from SR with a standard magnet

Fig. 14 summarizes the different kinds of particles encountered in the SS316L recycled powders, including as-virgin particles, elongated particles and agglomerates, partially oxidized particles, colored particles, magnetic particles and sieved residues. All the characteristics of the sieve residues presented in this study show the importance of the sieving stage, which is essential to limit the degradation of the feedstock during powder reuse in L-PBF.

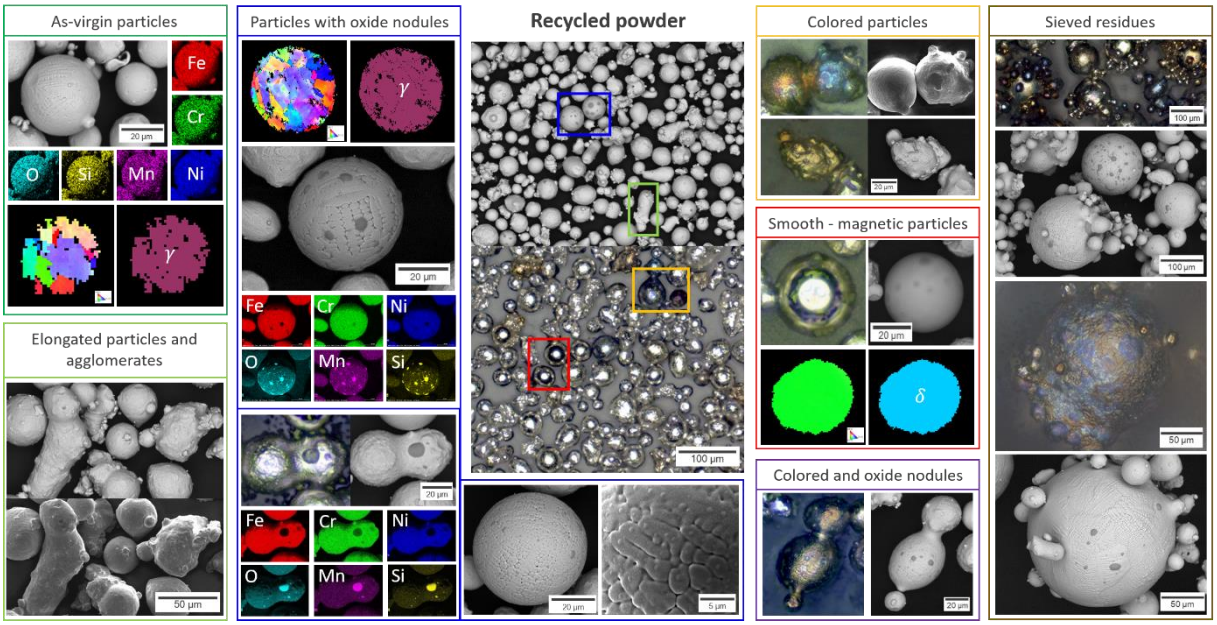

Fig. 14. Summary of particles present in the recycled powders

3.2. Effect of recycling on printed parts

In parallel with the characterization of the powders, parts manufactured during this recycling study were analyzed to follow potential changes regarding their metallurgical attributes, chemical composition and mechanical properties.

Metallurgical characterization of printed parts was performed with density and microstructure measurements. Fig. 15 represents the evolution of the cubic parts density measured by Archimedes method and metallographic observation. Archimedes density is rather stable during 5-6 printing cycles then decreases as powder reuse is pursued. On the other hand, image analyses of samples cross sections present very few porosities and remain constant over the 15 fabrications. However, this method assesses the components density on surface observations, which might not be representative of the whole part. Differences are not necessarily noticeable, especially when densities are really high and variations are minor. A first explanation to account for such a decrease is that surface oxidation present on recycled particles can increase the absorption of laser irradiation resulting in increased recoil pressure and surface tension variations [10]. This can cause more liquid metal to leak out as spatters, which can also create inclusions and pores when falling back on the parts. Another potential explanation for the observed density decrease of solidified samples density could be related to PSD increase. Larger particles need more energy to be melted and similar L-PBF processing conditions may lead to voids and inclusions. However, in view of the very limited size increases observed (see Fig. 4) such a mechanism does not appear as very likely.

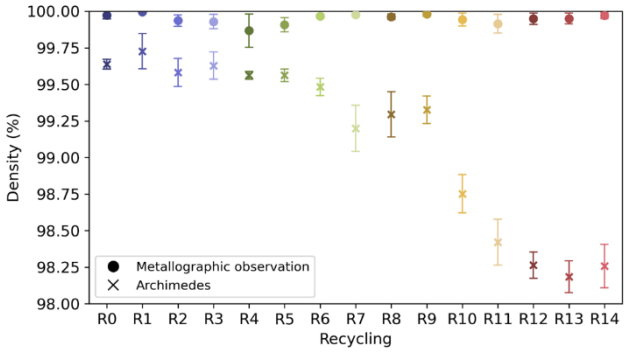

Fig. 15. Parts density measured by Archimedes method and metallographic observation in function of recycling

The microstructure of the cubic samples was observed by OM and SEM. Typical L-PBF microstructure is found with large colomnar grains, traces of melt pool boundaries and cellular network structures [48]. Grains are elongated and aligned with the building direction (parallel to z axis), extending across several melt pools. Fig. 16 provides EBSD grain maps in xz plane of cubic parts printed with virgin powder (R0), 7-times recycled (R7) and 14-times recycled (R14) powders. Grains are determined using a boundary misorientation angle of 5° on Quantax ESPRIT 2.0 Brukker software.

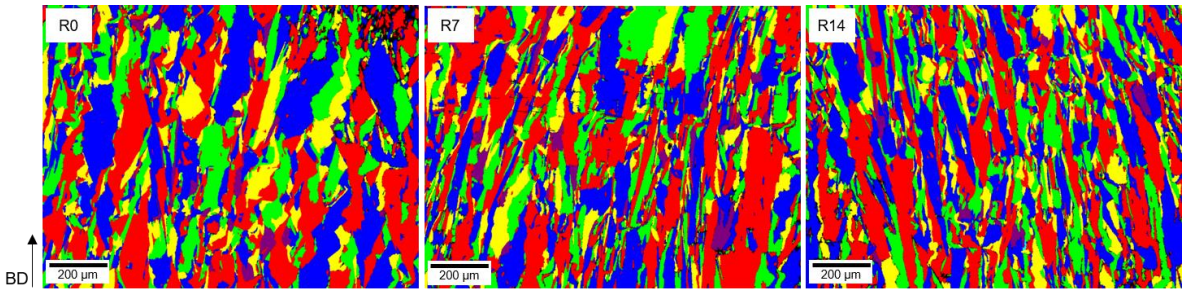

Fig. 16. ESBD grain maps of cross sections in building direction (BD) of R0, R7 and R14 cubic samples

It is apparent that the grains become more numerous and finer for parts manufactured with reused powders. Grain size and shape analyses confirms this visual impression, with the values of grains number, median size and average size corresponding to the three EBSD maps reported in Table 3. Grain sizes are calculated reported to the surface.

Table 3. Grains number, median and average sizes in EBSD maps of R0, R7 and R14 parts

Recycling	Grains number	Median size (µm)	Average size (µm)	Standard deviation (µm)
R0	1157	97.9	108.5	65.6
R7	1369	85.4	99.5	66.9
R14	1680	72.5	80.5	49.4

These changes in grains number and size could be explained by the increase in oxygen content in the recycled powders. It is expected in L-PBF printed parts that fairly uniform distribution of nano-oxides are found throughout the build, due to L-PBF processing conditions and oxygen from the powder [49]. Inclusions were found to be rich in O, Cr, and Si or O, Mn, N, Si and Al in the case of austenitic stainless steels by different authors [46][47]. Those inclusions may influence the microstructure of

the solidified samples in two possible ways. The oxides could act as nucleating sites for grain germination which promotes grain refinement [51]; and/or they could contribute to pinning of the grain boundaries and inhibit grain growth [52]. On the other hand, it can be recalled that the same process parameters were used for all fabrications, therefore the refinement cannot be attributed to a change in cooling rate. In addition, nucleant particles (*e.g.* ferrite) could be expected to impact grain size but none was ever observed in the elaborated parts.

Oxygen content was also measured by inert gas fusion on the solidified parts. Fig. 17 represents the oxygen concentrations in wppm of parts from the 15 L-PBF prints. As for the powders, there is a gradual increase throughout the powder reuse cycles. Both initial and final conditions remain lower in oxygen content than the powders, but the rise is still around 150 wppm over the 15 fabrications.

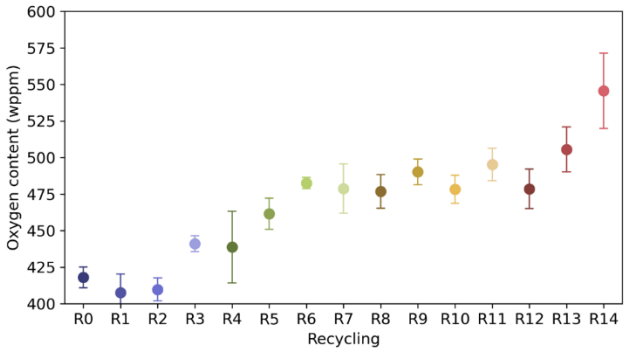

Fig. 17. Oxygen content in the printed parts with recycling

Mechanical properties of the parts were investigated. Microhardness tests showed no significant difference between the different reuse conditions (Fig. 18). The values are steady around 212 HV, with a standard deviation of 8 HV. The same trend is observed for the uniaxial tensile tests (Fig. 19). Yield strength (YS), ultimate tensile strength (UTS) and elongation at break remain stable with the increase of feedstock reuse, with satisfactory values of YS around 580 MPa, UTS around 670 MPa and ductility of 40 %, with standard deviations of 9 MPa, 8 MPa and 5 % respectively. These values compare favorably to mechanical properties of L-PBF processed SS316L given in the literature [5], and are well above the minimum UTS, YS and elongation requirements of 515 MPa, 205 MPa and 30% respectively specified in the ASTM F3184 norm [53]. As a matter of fact, such results a posteriori validate the choices made regarding the processing parameters.

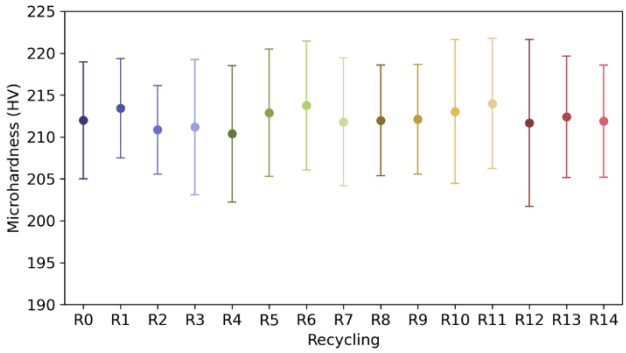

Fig. 18. Vickers microhardness of the printed parts with recycling

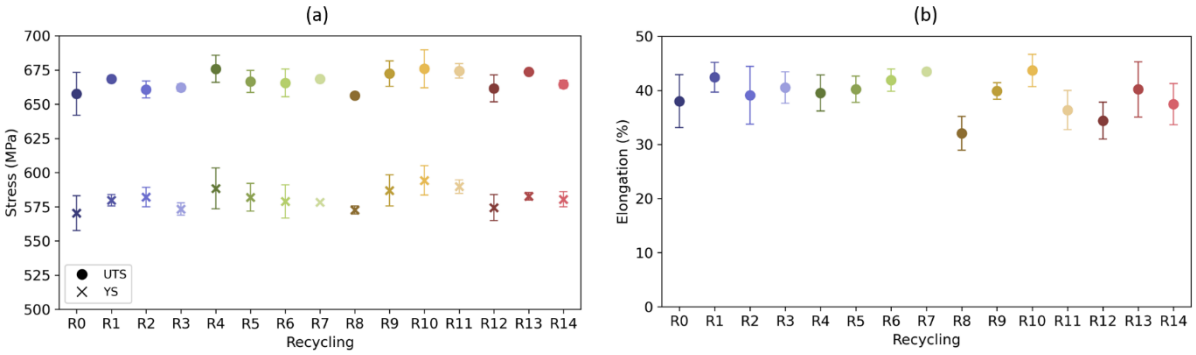

Fig. 19. (a) Ultimate tensile strength, yield strength, and (b) Elongation at break of printed parts with recycling

There is therefore no significant difference in mechanical strength, ductility and microhardness despite the grain refinement observed previously. It can be assumed that the large and elongated grains are not the major contribution to the tensile properties of the L-PBF parts, as it was claimed by Leicht et al. [54] and Wang et al. [4]. They assumed that variations of mechanical strength are mainly due to the fine cellular structure inside the grains. The cellular networks of the cubic samples were observed by SEM. However, the large variation of cell sizes within a cross section do not enable to determine average sizes and trends regarding the different prints.

4. Conclusions

In this study, gas-atomized 316L stainless steel powder was recycled 15 times in a standard L-PBF process. A thorough investigation of powder and parts properties was conducted after each printing cycle. The following conclusions can be drawn from this work:

- Powders show a slight increase in particle size with recycling, with the presence of irregular shaped particles in the feedstock even after sieving using a 50 µm mesh.
- Recycled powders exhibit an improved flowability, mainly due to an increased presence of particles with surface oxidation.
- The oxygen content of both powder and printed parts gradually increases with reuse time, from 475 to 675 wppm and 405 to 545 wppm respectively after 15 builds. No other significant changes are found in recycled powder chemical composition.
- Partially oxidized spatter particles with Mn and Si rich oxide nodules are present in recycled powders even after the sieving process. The latter could be vapor-entrained particles that oxidized in flight. A major increase of colored particles (yellow-brown, blue) is also noticeable after several reuses, due to their presence in heat-affected zones near the vicinity of solidified parts.
- A significant amount of δ-ferrite (4 wt.%) is found in the 15-times recycled powder after sieving, compared to the almost fully austenitic virgin powder (0-1 wt.% of BCC ferrite). Also present in great amount in the sieve residues due to magnetic interactions and clustering, these highly spherical particles do not exceed 70-80 µm and solidify under supercooling condition in single crystal ferrite.
- The sieving process is crucial to limit powder degradation and L-PBF process alteration with powder reuse, as it discards large agglomerates and magnetic particles with high oxygen content (around 1800 wppm). However, it does not remove all altered particles as presented above, which can alter future fabrications.
- Parts density remain rather stable during 5-6 fabrications then decreases progressively.
- Parts microstructure highlight grain refinements over the L-PBF prints, with more numerous and finer grains possibly coming from oxide inclusions acting as nucleation sites or contributing to the pinning of the grain boundaries.
- There is no significant difference in samples microhardness and tensile properties with powder recycling. SS136L powder can thus be used up to 15 times with the L-PBF process without significantly compromising mechanical properties of elaborated specimens.

The results from this study show that SS316L powder is altered during the L-PBF process and its multiple reuse leads to changes in particles morphology, composition and crystallographic phases, although the sieving process between each fabrication strongly contributes to the limitation of these variations. Tensile properties and microhardness remain satisfactory, but changes in parts density and microstructure are significant. A third method, X-ray tomography, will be assessed in the future to compare and validate the porosity measurements performed by metallographic observations and the Archimedes method. Further investigations should explore the grains modifications in recycled part and the potential of grain refinement with oxidized powders. Moreover, additional mechanical properties such as fatigue and impact toughness analyses should be implemented regarding the evolution of parts density and oxygen content observed in this study. In addition to conventional vibrating sieving, a step of magnetic separation could be added between reuse cycles in order to counteract the tendency for ferrite particles accumulation. Finally, it would be interesting to investigate L-PBF process related variables that could have an impact on powder degradation, as the

influence of parts spacing or shield gas protection. This could expand the understanding of powder recycling, limit powder alteration phenomena and therefore increase material yield in L-PBF.

CRediT authorship contribution statement

Timothée Delacroix: Methodology, Validation, Investigation, Writing - original draft, Writing - review & editing, Visualization. **Fernando Lomello:** Conceptualization, Writing – review & editing, Supervision. **Frédéric Schuster:** Conceptualization, Funding acquisition. **Hicham Maskrot:** Resources, Project administration. **Jean-Paul Garandet:** Conceptualization, Writing – review & editing, Supervision.

Declaration of Competing Interest

The authors declare that they have no known competing financial interests or personal relationships that could have appeared to influence the work reported in this paper.

Acknowledgments

The authors gratefully acknowledge the technical and financial support provided by the CEA Cross-Cutting Program on Materials and Processes Skills, France.

References

[1] ASTM, ISO - ASTM52900-15 Standard Terminology for Additive Manufacturing – General Principles – Terminology, ASTM International, West Conshohocken, PA, (2015). https://doi.org/10.1520/ISOASTM52900-15.

[2] N. Guo, M.C. Leu, Additive manufacturing: technology, applications and research needs, Front. Mech. Eng. 8 (2013) 215–243. https://doi.org/10.1007/s11465-013-0248-8.

[3] W.E. Frazier, Metal Additive Manufacturing: A Review, J. Mater. Eng. Perform. 23 (2014) 1917–1928. https://doi.org/10.1007/s11665-014-0958-z.

[4] Y.M. Wang, T. Voisin, J.T. McKeown, J. Ye, N.P. Calta, Z. Li, Z. Zeng, Y. Zhang, W. Chen, T.T. Roehling, R.T. Ott, M.K. Santala, P.J. Depond, M.J. Matthews, A.V. Hamza, T. Zhu, Additively manufactured hierarchical stainless steels with high strength and ductility, Nat. Mater. 17 (2018) 63–71. https://doi.org/10.1038/nmat5021.

[5] T. Kurzynowski, K. Gruber, W. Stopyra, B. Kuźnicka, E. Chlebus, Correlation between process parameters, microstructure and properties of 316 L stainless steel processed by selective laser melting, Mater. Sci. Eng. A. 718 (2018) 64–73. https://doi.org/10.1016/j.msea.2018.01.103.

[6] C. Galy, E. Le Guen, E. Lacoste, C. Arvieu, Main defects observed in aluminum alloy parts produced by SLM: From causes to consequences, Addit. Manuf. 22 (2018) 165–175. https://doi.org/10.1016/j.addma.2018.05.005.

[7] J. Zhang, B. Song, Q. Wei, D. Bourell, Y. Shi, A review of selective laser melting of aluminum alloys: Processing, microstructure, property and developing trends, J. Mater. Sci. Technol. 35 (2019) 270–284. https://doi.org/10.1016/j.jmst.2018.09.004.

[8] T. DebRoy, H.L. Wei, J.S. Zuback, T. Mukherjee, J.W. Elmer, J.O. Milewski, A.M. Beese, A. Wilson-Heid, A. De, W. Zhang, Additive manufacturing of metallic components – Process, structure and properties, Prog. Mater. Sci. 92 (2018) 112–224. https://doi.org/10.1016/j.pmatsci.2017.10.001.

[9] J.M. Benson, E. Snyders, The need for powder characterisation in the additive manufacturing industry and the establishment of a national facility, South Afr. J. Ind. Eng. 26 (2015) 104–114. https://doi.org/10.7166/26-2-951.
[10] A. Simchi, The role of particle size on the laser sintering of iron powder, Metall. Mater. Trans. B. 35 (2004) 937–948. https://doi.org/10.1007/s11663-004-0088-3.
[11] S. Cacace, A.G. Demir, Q. Semeraro, Densification Mechanism for Different Types of Stainless Steel Powders in Selective Laser Melting, Procedia CIRP. 62 (2017) 475–480. https://doi.org/10.1016/j.procir.2016.06.010.
[12] A.B. Spierings, G. Levy, Comparison of density of stainless steel 316L parts produced with Selective Laser Melting using different powder grades, 20th Annu. Int. Solid Free. Fabr. Symp. SFF 2009. (2009) 342–353.
[13] M. Baumers, C. Tuck, R. Wildman, I. Ashcroft, E. Rosamond, R. Hague, Combined build-time, energy consumption and cost estimation for direct metal laser sintering, 23rd Annu. Int. Solid Free. Fabr. Symp. - Addit. Manuf. Conf. SFF 2012. (2012) 932–944.
[14] J. Teubler, S. Weber, P. Suski, I. Peschke, C. Liedtke, Critical evaluation of the material characteristics and environmental potential of laser beam melting processes for the additive manufacturing of metallic components, J. Clean. Prod. 237 (2019) 117775. https://doi.org/10.1016/j.jclepro.2019.117775.
[15] M. Barclift, S. Joshi, T.W. Simpson, C.J. Dickman, Cost Modeling and Depreciation for Reused Powder Feedstocks in Powder Bed Fusion Additive Manufacturing, Proc. 27th Annu. Int. Solid Free. Fabr. Symp. SFF 2016. (2016) 2007–2028.
[16] S.A. Khairallah, A.T. Anderson, A. Rubenchik, W.E. King, Laser powder-bed fusion additive manufacturing: Physics of complex melt flow and formation mechanisms of pores, spatter, and denudation zones, Acta Mater. 108 (2016) 36–45. https://doi.org/10.1016/j.actamat.2016.02.014.
[17] Y. Liu, Y. Yang, S. Mai, D. Wang, C. Song, Investigation into spatter behavior during selective laser melting of AISI 316L stainless steel powder, Mater. Des. 87 (2015) 797–806. https://doi.org/10.1016/j.matdes.2015.08.086.
[18] M. Lutter-Günther, M. Bröker, T. Mayer, S. Lizak, C. Seidel, G. Reinhart, Spatter formation during laser beam melting of AlSi10Mg and effects on powder quality, Procedia CIRP. 74 (2018) 33–38. https://doi.org/10.1016/j.procir.2018.08.008.
[19] D. Wang, S. Wu, F. Fu, S. Mai, Y. Yang, Y. Liu, C. Song, Mechanisms and characteristics of spatter generation in SLM processing and its effect on the properties, Mater. Des. 117 (2017) 121–130. https://doi.org/10.1016/j.matdes.2016.12.060.
[20] F.C. Pinto, I.R. Souza Filho, M.J.R. Sandim, H.R.Z. Sandim, Defects in parts manufactured by selective laser melting caused by δ-ferrite in reused 316L steel powder feedstock, Addit. Manuf. 31 (2020) 100979. https://doi.org/10.1016/j.addma.2019.100979.
[21] V. Seyda, N. Kaufmann, C. Emmelmann, Investigation of Aging Processes of Ti-6Al-4 V Powder Material in Laser Melting, Phys. Procedia. 39 (2012) 425–431. https://doi.org/10.1016/j.phpro.2012.10.057.
[22] J. Slotwinski, E. Garboczi, P. Stutzman, C. Ferraris, S. Watson, M. Peltz, Characterization of Metal Powders Used for Additive Manufacturing, J. Res. Natl. Inst. Stand. Technol. 119 (2014) 460–493. https://doi.org/10.6028/jres.119.018.
[23] F. Ahmed, U. Ali, D. Sarker, E. Marzbanrad, K. Choi, Y. Mahmoodkhani, E. Toyserkani, Study of powder recycling and its effect on printed parts during laser powder-bed fusion of 17-4 PH stainless steel, J. Mater. Process. Technol. (2019) 116522. https://doi.org/10.1016/j.jmatprotec.2019.116522.
[24] A.T. Sutton, C.S. Kriewall, S. Karnati, M.C. Leu, J.W. Newkirk, Characterization of AISI 304L stainless steel powder recycled in the laser powder-bed fusion process, Addit. Manuf. 32 (2020) 100981. https://doi.org/10.1016/j.addma.2019.100981.

[25] P.E. Carrion, A. Soltani-Tehrani, N. Phan, N. Shamsaei, Powder Recycling Effects on the Tensile and Fatigue Behavior of Additively Manufactured Ti-6Al-4V Parts, JOM. 71 (2018) 963–973. https://doi.org/10.1007/s11837-018-3248-7.
[26] L. Cordova, M. Campos, T. Tinga, Revealing the Effects of Powder Reuse for Selective Laser Melting by Powder Characterization, JOM. 71 (2019) 1062–1072. https://doi.org/10.1007/s11837-018-3305-2.
[27] H.P. Tang, M. Qian, N. Liu, X.Z. Zhang, G.Y. Yang, J. Wang, Effect of Powder Reuse Times on Additive Manufacturing of Ti-6Al-4V by Selective Electron Beam Melting, JOM. 67 (2015) 555–563. https://doi.org/10.1007/s11837-015-1300-4.
[28] P. Nandwana, W.H. Peter, R.R. Dehoff, L.E. Lowe, M.M. Kirka, F. Medina, S.S. Babu, Recyclability Study on Inconel 718 and Ti-6Al-4V Powders for Use in Electron Beam Melting, Metall. Mater. Trans. B. 47 (2016) 754–762. https://doi.org/10.1007/s11663-015-0477-9.
[29] M.J. Heiden, L.A. Deibler, J.M. Rodelas, J.R. Koepke, D.J. Tung, D.J. Saiz, B.H. Jared, Evolution of 316L stainless steel feedstock due to laser powder bed fusion process, Addit. Manuf. 25 (2019) 84–103. https://doi.org/10.1016/j.addma.2018.10.019.
[30] A.T. Sutton, C.S. Kriewall, M.C. Leu, J.W. Newkirk, B. Brown, Characterization of laser spatter and condensate generated during the selective laser melting of 304L stainless steel powder, Addit. Manuf. 31 (2020) 100904. https://doi.org/10.1016/j.addma.2019.100904.
[31] M. Simonelli, C. Tuck, N.T. Aboulkhair, I. Maskery, I. Ashcroft, R.D. Wildman, R. Hague, A Study on the Laser Spatter and the Oxidation Reactions During Selective Laser Melting of 316L Stainless Steel, Al-Si10-Mg, and Ti-6Al-4V, Metall. Mater. Trans. A. 46 (2015) 3842–3851. https://doi.org/10.1007/s11661-015-2882-8.
[32] B. Sartin, T. Pond, B. Griffith, W. Everhart, L. Elder, E. Wenski, C. Cook, D. Wieliczka, W. King, A. Rubenchik, S. Wu, B. Brown, C. Johnson, J. Crow, 316L powder reuse for metal additive manufacturing, Solid Free. Fabr Symp Proc. 2017 (2017) 351–364.
[33] G. Jacob, C.U. Brown, M.A. Donmez, S.S. Watson, J. Slotwinski, Effects of powder recycling on stainless steel powder and built material properties in metal powder bed fusion processes, National Institute of Standards and Technology, Gaithersburg, MD, 2017. https://nvlpubs.nist.gov/nistpubs/ams/NIST.AMS.100-6.pdf.
[34] A. Strondl, O. Lyckfeldt, H. Brodin, U. Ackelid, Characterization and Control of Powder Properties for Additive Manufacturing, JOM. 67 (2015) 549–554. https://doi.org/10.1007/s11837-015-1304-0.
[35] ASTM A240 / A240M-20a, Standard Specification for Chromium and Chromium-Nickel Stainless Steel Plate, Sheet, and Strip for Pressure Vessels and for General Applications, ASTM International, West Conshohocken, PA, 2020. https://doi.org/10.1520/A0240_A0240M-20A.
[36] L. Lutterotti, Maud Version 2.94, 2020. http://maud.radiographema.eu/.
[37] ASTM B212-17, Standard Test Method for Apparent Density of Free-Flowing Metal Powders Using the Hall Flowmeter Funnel, ASTM International, West Conshohocken, PA, 2017. https://doi.org/10.1520/B0212-17.
[38] T. de Terris, O. Andreau, P. Peyre, F. Adamski, I. Koutiri, C. Gorny, C. Dupuy, Optimization and comparison of porosity rate measurement methods of Selective Laser Melted metallic parts, Addit. Manuf. 28 (2019) 802–813. https://doi.org/10.1016/j.addma.2019.05.035.
[39] ISO 6892-1, Metallic materials - Tensile testing - Part 1: Method of test at room temperature, 2019. https://www.iso.org/standard/78322.html.
[40] N.P. Karapatis, G. Egger, P.E. Gygax, R. Glardon, Optimization of Powder Layer Density in Selective Laser Sintering, in: 1999. http://dx.doi.org/10.26153/tsw/746.
[41] K. Abd-Elghany, D.L. Bourell, Property evaluation of 304L stainless steel fabricated by selective laser melting, Rapid Prototyp. J. (2012). https://doi.org/10.1108/13552541211250418.
[42] J.H. Tan, W.L.E. Wong, K.W. Dalgarno, An overview of powder granulometry on feedstock and part performance in the selective laser melting process, Addit. Manuf. 18 (2017) 228–255. https://doi.org/10.1016/j.addma.2017.10.011.

[43] J. Ki Leuk Lai, K. Ho Lo, C. Hung Shek, eds., Chapter 12 - Colouration of Stainless Steels, in: Stainl. Steels Introd. Their Recent Dev., BENTHAM SCIENCE PUBLISHERS, 2012: p. 151. https://doi.org/10.2174/9781608053056112010 1.
[44] S. Ly, A.M. Rubenchik, S.A. Khairallah, G. Guss, M.J. Matthews, Metal vapor micro-jet controls material redistribution in laser powder bed fusion additive manufacturing, Sci. Rep. 7 (2017) 1–12. https://doi.org/10.1038/s41598-017-04237-z.
[45] P.S. Korinko, S.H. Malene, Considerations for the weldability of types 304L and 316L stainless steel, Pract. Fail. Anal. 1 (2001) 61–68. https://doi.org/10.1007/BF02715336.
[46] D. Kotecki, T. Siewert, WRC-1992 constitution diagram for stainless steel weld metals : a modification of the WRC-1988 diagram, Weld. J. 71 (1992). http://files.aws.org/wj/supplement/WJ_1992_05_s171.pdf.
[47] Z.A. Young, Q. Guo, N.D. Parab, C. Zhao, M. Qu, L.I. Escano, K. Fezzaa, W. Everhart, T. Sun, L. Chen, Types of spatter and their features and formation mechanisms in laser powder bed fusion additive manufacturing process, Addit. Manuf. 36 (2020) 101438. https://doi.org/10.1016/j.addma.2020.101438.
[48] A. Leicht, M. Rashidi, U. Klement, E. Hryha, Effect of process parameters on the microstructure, tensile strength and productivity of 316L parts produced by laser powder bed fusion, Mater. Charact. (2019) 110016. https://doi.org/10.1016/j.matchar.2019.110016.
[49] K. Saeidi, X. Gao, Y. Zhong, Z.J. Shen, Hardened austenite steel with columnar sub-grain structure formed by laser melting, Mater. Sci. Eng. A. 625 (2015) 221–229. https://doi.org/10.1016/j.msea.2014.12.018.
[50] Q. Chao, V. Cruz, S. Thomas, N. Birbilis, P. Collins, A. Taylor, P.D. Hodgson, D. Fabijanic, On the enhanced corrosion resistance of a selective laser melted austenitic stainless steel, Scr. Mater. 141 (2017) 94–98. https://doi.org/10.1016/j.scriptamat.2017.07.037.
[51] Ø. Grong, L. Kolbeinsen, C. van der Eijk, G. Tranell, Microstructure Control of Steels through Dispersoid Metallurgy Using Novel Grain Refining Alloys, ISIJ Int. 46 (2006) 824–831. https://doi.org/10.2355/isijinternational.46.824.
[52] F. Yan, W. Xiong, E. Faierson, G.B. Olson, Characterization of nano-scale oxides in austenitic stainless steel processed by powder bed fusion, Scr. Mater. 155 (2018) 104–108. https://doi.org/10.1016/j.scriptamat.2018.06.011.
[53] ASTM F3184-16, Standard Specification for Additive Manufacturing Stainless Steel Alloy (UNS S31603) with Powder Bed Fusion, ASTM International, West Conshohocken, PA, 2016. https://doi.org/10.1520/F3184-16.
[54] A. Leicht, C.H. Yu, V. Luzin, U. Klement, E. Hryha, Effect of scan rotation on the microstructure development and mechanical properties of 316L parts produced by laser powder bed fusion, Mater. Charact. 163 (2020) 110309. https://doi.org/10.1016/j.matchar.2020.110309.